communications chemistry

A Nature Portfolio journal

Article

https://doi.org/10.1038/s42004-026-01985-w

Hydrogen evolution electrocatalysts in high-fold degenerate topological semimetals with chiral structures

Yan Wang[1], Heshan Yu[2], Qiunan Xu[1] ✉ & Wenjian Liu[1]

Topological catalysts are special class of high-activity catalysts that have topological surface state with high-mobility electrons to promote electron transfer. Among topological materials, high-fold degenerate topological semimetals (TSMs) with chiral structures are particularly effective in hydrogen evolution reaction (HER) catalysis due to the larger energy window of nontrivial surface states and longer Fermi arcs than other classes. In this work, based on high-throughput calculations and the database of high-fold degenerate TSMs with chiral structures that we have established, we predict 16 high-activity topological catalysts with Gibbs free energy |ΔG| smaller than that of Pt. Among them, PtGa and PtPbTe with space group $P2_13$ and $Pd_3Pb_2S_2$ with space group $I2_13$ exhibit outstanding catalytic behavior. Furthermore, by comparing the adsorption energy on the surfaces with and without topological surface state in the same compound straightly, the substantive fact that the extremely long topological surface state provides virtual improvement of HER catalytic performance is verified. Thus, this work not only discovers a lot of HER topological catalysts, but also provides and corroborates an innovative strategy to design high-activity catalysts, i.e., constructing monometallic catalysts into TSMs.

Global environmental problems and energy crisis are two of the most serious problems facing humanity[1–3]. Therefore, hydrogen energy, as a clean and sustainable energy, has received unprecedented attention[4,5]. In contrast with steam methane reforming[6], which also emits a mass of CO_2, water decomposition[7,8] is a cleaner and easier way to produce hydrogen. However, the energy consumption required for water electrolysis is very high, making the development of high-efficiency and stable catalysts particularly necessary. The hydrogen evolution reaction (HER) is precisely the half-reaction that produces hydrogen in water electrolysis, and the design of high-activity catalysts for HER indeed enhances the activity of water splitting and effectively reduces energy consumption[9,10]. In general, regulating the adsorption behavior of intermediates such as *H can promote the electron transfer directly and be used to improve catalytic activity. At present, the volcano plot[11] which correlates the electrocatalytic efficiency with the Gibbs free energy ΔG has been widely used to reveal the activity of HER catalysts. The Gibbs free energy of hydrogen adsorption on the surface of an efficient HER catalyst is close to zero, i.e., at the peak of the volcano plot. The well-known high-activity HER catalysts Pt and Pd both follow this rule, but their high prices prompt people to seek alternatives.

Besides single-atom catalysts[12,13], heterostructures[14], and alloying[15] can reduce the cost, topological materials, including topological insulators (TIs)[16–18] and topological semimetals (TSMs)[19,20] are also excellent candidates for HER catalysts[21–25]. TI is insulated internally, while its surface is conductive. The electronic properties of TSMs are similar to those of TIs, except that its bulk band structures have band crossing points near Fermi level, which makes it behave as a semimetal internally. According to the degeneracy of the band crossing points known as topological points, TSMs can be divided into four categories: Weyl TSMs[26–33], Dirac TSMs[34,35], nodal-line TSMs[36], and high-fold degenerate TSMs[37,38]. Therefore, they all have nontrivial topological surface states with high-mobility electrons moving along unidirectional conduction channels. The topological surface states are protected by bulk crystal symmetries and robust against backscattering. The high-mobility electrons and stability are exactly what HER catalysis requires, and the crucial role of topological surface states in facilitating surface electrochemical reactions has been demonstrated by serving as an effective electron bath[39]. Recently, nonmagnetic Weyl TSMs TaAs family of materials[40], nodal-line TSMs TiSi family of materials[41], Dirac TSM $PtSn_4$[42], ferromagnetic Weyl TSM $Co_3Sn_2S_2$[43], type-II Weyl TSMs $W/MoTe_2$[44,45], and several high-fold degenerate TSMs with chiral structures, such as PtGa/

[1]Qingdao Institute for Theoretical and Computational Sciences, Center for Optics Research and Engineering, Shandong University, Qingdao, China. [2]School of Microelectronics, Tianjin University, Tianjin, China. ✉e-mail: xuqiunan91@email.sdu.edu.cn

Al[46], CoSi[47], NiSi[48], and TcSi[49], are predicted as high-activity HER topological catalysts theoretically. However, only a few topological catalysts have been verified in experiment, and Pt remains the most efficient catalyst for applications. Among the limited number of topological catalysts, the high-fold degenerate TSMs with chiral structures show remarkable potential in catalysis. Due to the lack of mirror and inversion symmetry, the nontrivial topological points with nonzero Chern number in TSMs with chiral structures locate at different energy, making the energy window of nontrivial states larger. According to the experimental study of PtGa and PtAl[46], which have better HER catalytic performance than Pt, this large energy window of nontrivial states plays an important role in enhancing the catalytic activity. Therefore, it is expected to discover more efficient topological catalysts in high-fold degenerate TSMs with chiral structures.

In this work, in order to explore high-activity HER topological catalysts through high-throughput screening founded on the first-principles calculations, based on the database of high-fold degenerate TSMs with chiral structures that we have established in previous work[50], we focus on TSMs with the same point group T as CoSi family of materials, only a few of which have been theoretically and experimentally predicted as excellent HER catalysts[51,52]. We have not only verified the high catalytic performance of PtGa and PtAl in experiment, but also predicted that the catalytic activity of PtPbTe and $Pd_3Pb_2S_2$ is not inferior to them. In addition, a large number of topological catalysts with good catalytic performance, such as PtBiTe, NiPS, and $Pd_3Bi_2S_2$, have also been discovered. Totally 16 high-fold degenerate topological catalysts, whose Gibbs free energies |ΔG| are smaller than the calculated |ΔG| of Pt (i.e., 0.156 eV), are explored. More importantly, in the same compound, the surface with topological surface states can provide higher catalytic activity than the surface without topological surface states, which directly verifies the positive impact of topological surface states with high-mobility electrons on HER catalysis. Thus, this work not only provides more promising topological catalysts for HER catalysis but also proposes an effective method for developing high-activity catalysts.

Results and discussion

Among the 146 nonmagnetic high-fold degenerate TSMs with chiral structures discovered in our previous work[50], we focus on 82 TSMs having the same point group T with CoSi family of materials to investigate the impact of topological states on topological catalysis and explore more high-activity HER topological catalysts. Since the adsorption calculations on the surface of supercell require a lot of computational resources, the TSMs having too many atoms (more than 20 atoms per unit cell) are not considered for the time being. Therefore, we obtain 47 high-fold degenerate TSM candidates, including 42 TSMs with space group $P2_13$ (No. 198) and 5 TSMs with space group $I2_13$ (No. 199), whose lattice constants are shown in Supplementary Tables S1–2 and Supplementary Figs. S1–3.

According to the crystal structures, we classify them into three types: the binary compounds with space group $P2_13$, the ternary compounds with space group $P2_13$, and the compounds with space group $I2_13$. The CoSi family of materials is all in the first type. To better exhibit the crystal structures, as shown in Fig. 1, PtGa, PtPbTe, and $Pd_3Pb_2S_2$, which respectively have 8, 12, and 14 atoms per unit cell, are chosen as representatives of these three types. Since all the compounds belong to the same point group T (or 23 in international symbols), they manifest three kinds of symmetry operations: three-fold rotation symmetry with [111] axis, two-fold screw rotation symmetry with [100], [010] and [001] axes, and three-fold screw rotation symmetry with $[1\bar{1}\bar{1}]$, $[\bar{1}1\bar{1}]$ and $[\bar{1}\bar{1}1]$ axes. The high-fold degenerate points located at the high-symmetry k-points are marked in the band structures in Figs. 1i–k. For compounds with space group $P2_13$ like PtGa and PtPbTe, two four-fold degenerate points $H^{\Gamma}_{PG/PPT}$ and $H^{M}_{PG/PPT}$ with Chern number −4 and ±2 locate at Γ and M points, respectively, while the Chern number of six-fold degenerate point $H^{R}_{PG/PPT}$ at R point is +4. The

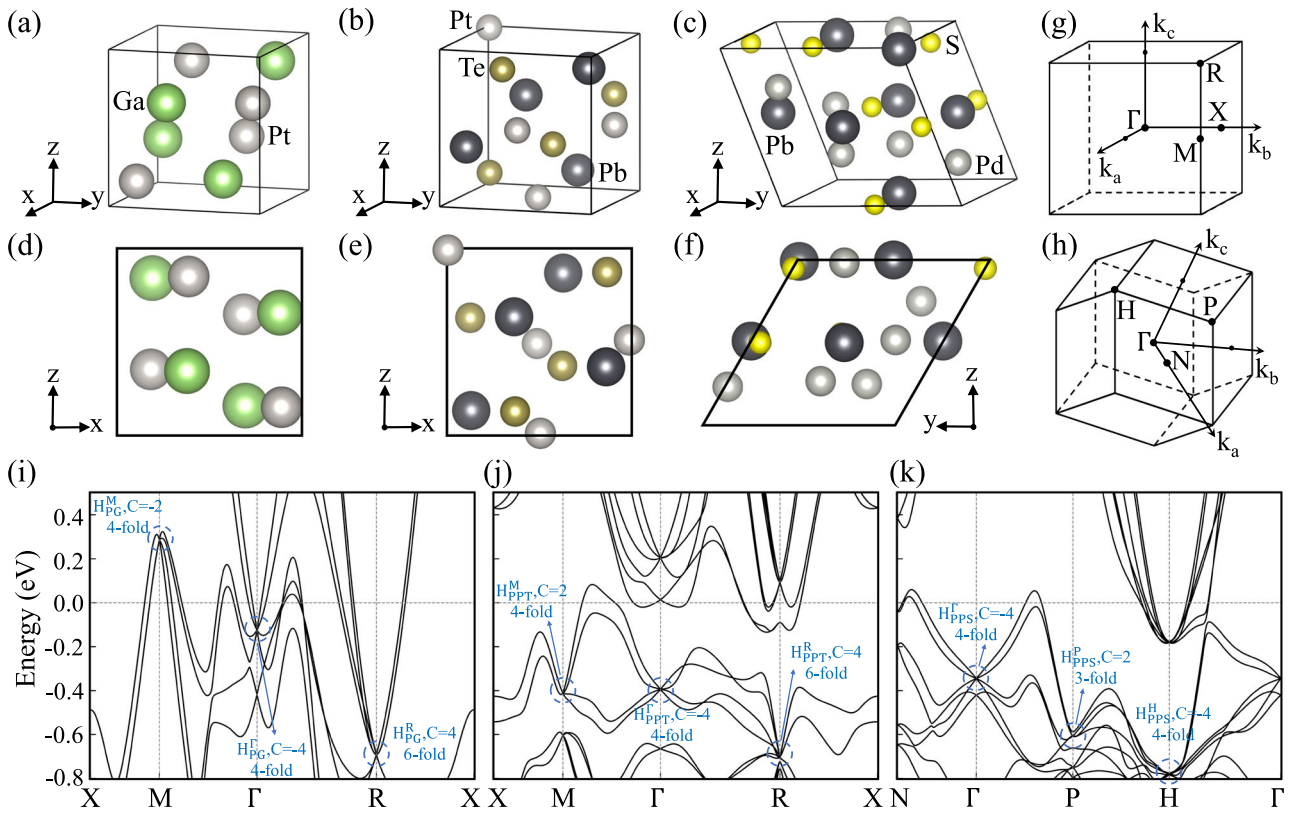

Fig. 1 | Crystal and band structures of the high-fold degenerate topological semimetals (HDTMs). a–c Lattice structure of binary HDTMs with space group $P2_13$ (No. 198), ternary HDTMs with space groups $P2_13$ (No. 198) and HDTMs with space group $I2_13$ (No. 199), respectively. **d–f** Side view of the lattice structure in **a–c**. **g, h** Brillouin zone of space group $P2_13$ and $I2_13$. **i–k** Band structure of PtGa with space group $P2_13$, PtPbTe with space group $P2_13$, and $Pd_3Pb_2S_2$ with space group $I2_13$, respectively.

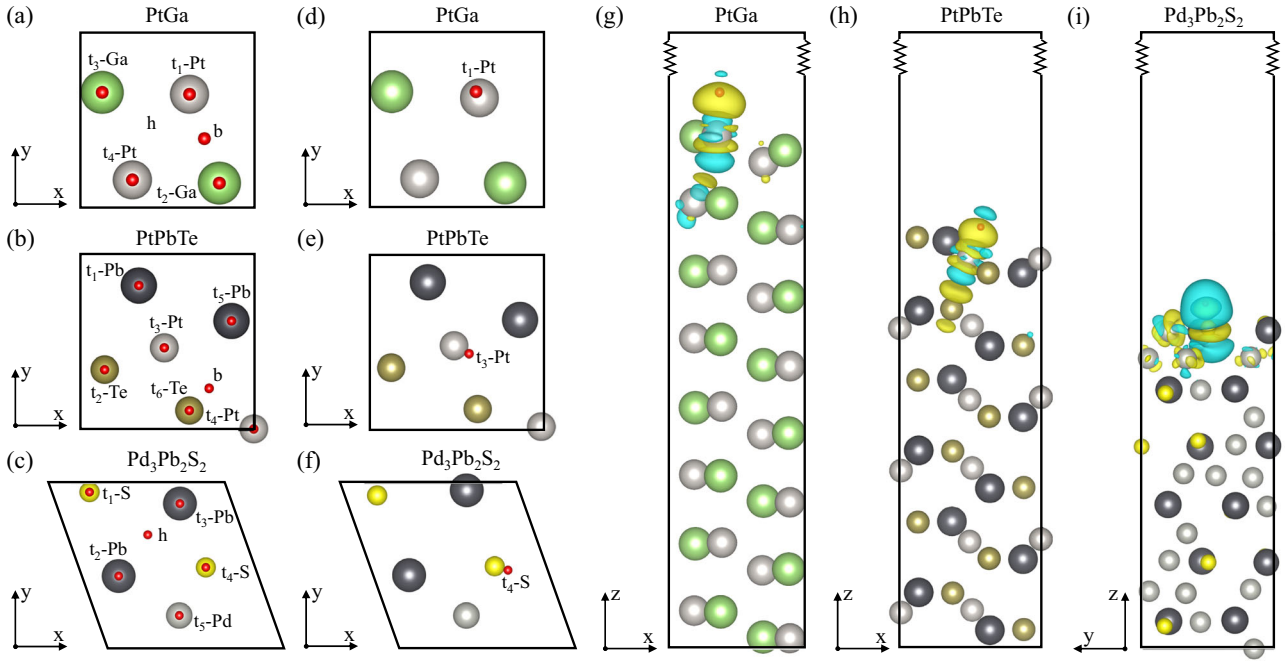

Fig. 2 | Adsorption site for H atom and differential charge density after adsorption. a–c The potential adsorption sites in PtGa, PtPbTe, and $Pd_3Pb_2S_2$, respectively. t/b/h represents top/bridge/hollow site. **d–f** The most stable adsorption sites in PtGa, PtPbTe, and $Pd_3Pb_2S_2$. Only one layer of atoms is shown in the top views. **g–i** The differential charge density of PtGa, PtPbTe, and $Pd_3Pb_2S_2$ when H atom is adsorbed. The yellow/blue surfaces represent the increasing/decreasing of density of electrons. All red balls are H atoms.

compounds with space group $I2_13$ can also host three-fold degenerate point H^P_{PPS} with Chern number +2 at P point and two four-fold degenerate points H^Γ_{PPS} and H^H_{PPS} with Chern number ± 4 at Γ and H, respectively.

For HER catalysis, the adsorption of H atoms on the surface of a solid plays a decisive role in the reaction. In order to construct the adsorption surface, we test all the possible surfaces of PtGa, PtPbTe, and $Pd_3Pb_2S_2$ in Supplementary Fig. S4. The differences in the surface energy are not significant for each compound, but comparatively speaking, the (001) surface possessing topological surface states is most stable. Therefore, we mainly focus on the HER on (001) adsorption surface when discussing the catalytic performance of the high-fold degenerate TSMs candidates.

The distribution of adsorption sites has a significant impact on the efficiency, selectivity, and performance of catalytic reactions in the adsorption process. Accordingly, we construct slab models with vacuum space along the [001] direction for each compound, and consider all possible adsorption configurations to identify the optimal adsorption sites for H atoms, which is shown in Figs. 2a–c. After the atoms on surface and adsorbed H have fully relaxed, the most stable adsorption sites for three representatives are shown in Figs. 2d–f, while the other high-fold degenerate TSM candidates can be found in Supplementary Figs. S8–S10. There are totally 36 TSM candidates possessing top adsorption sites, most of which are located at the top of transition metals due to the effect of d orbits, such as PtGa shown in Fig. S14. Meanwhile, the bridge sites exist in 11 TSM candidates, and the adsorbed H shifts towards top site slightly in most of them. As a whole, the top site is most stable for the compounds with T point group. If the candidate contains Pt, the top site of Pt is the optimal choice for adsorption, such as in representatives PtGa and PtPbTe. Besides, the top site of S is another choice when Pt is not contained, such as in representative $Pd_3Pb_2S_2$.

After determining the optimal adsorption site, the differential charge density of adsorption of H atoms is calculated to determine the transfer of electrons. As shown in Figs. 2g, h, the representatives PtGa and PtPbTe, in which H atom is adsorbed at the top of the transition metal Pt, the electrons transfer from Pt to H evidently. A few atoms in the next layer are also getting involved in the process of adsorption, which affects the direction of bonding. Similarly, all TSM candidates transfer the electrons from atoms on surface to adsorbate H atom except CuSeX (X=S or Te) with space group $P2_13$ and $A_3B_2S_2$ (A=Ni or Pd, B=Bi or Pb) with space group $I2_13$, which is shown in Supplementary Figs. S11–13. For example, in the representative $Pd_3Pb_2S_2$, H is adsorbed at the top of nonmetallic element S, the electronic distribution around H and S atoms changes complicatedly as depicted in Fig. 2i. The charge density increases near H and S atoms, and at the same time, the distribution of charge surrounding H atom is narrowed down. The transition metal Pd on surface also contributes electrons during the transferring process, although H is not adsorbed at the top of Pd atoms directly. Other $A_3B_2S_2$ compounds with space group $I2_13$ have the same characteristics with $Pd_3Pb_2S_2$. Therefore, for all of the high-fold degenerate TSMs candidates, adsorbate H atoms obtain electrons from atoms on surface, and transition metals also play an important role if they are included.

Subsequently, based on the adsorption site that is most stable in energy, the catalytic efficiency of HER for all the TSM candidates is characterized by the adsorption energy and displayed in the volcano plots of three TSM types in Fig. 3. The hydrogen adsorption Gibbs free energy ΔG for each TSM candidate is calculated by Eq. 2. Firstly, for binary TSM candidates with space group $P2_13$ (i.e., typical high-fold degenerate TSMs CoSi family of materials), there are seven compounds TcSi, PtGa, PtAl, CoGe, CoSi, RhSn and NiSi showing better catalytic performance than Pt as illustrated in Fig. 3a. If considering the deviation of Gibbs free energy between calculation in this work and experiment in Ref. 11, the catalytic performance of PtGa, PtAl, CoGe and CoSi are also superior to that of Pt. Among them, PtGa and PtAl have already been verified to have lower overpotential, lower Tafel slope, higher turnover frequency (TOF), and higher HER operational stability than Pt in experiment[46]. Besides PtGa and PtAl, TcSi[49], CoSi[47], and NiSi[48] have also been theoretically proposed to have good HER catalytic activity. All these results show that our high-throughput calculation on HER topological catalysts is reliable enough to explore high-activity catalysts. Secondly, among the ternary TSM candidates with space groups $P2_13$, which have been experimentally verified as high-fold degenerate TSMs[53], 7 compounds display better catalytic performance than Pt in calculation, while 6 compounds are demonstrated to have better performance than Pt in experiment as shown in Fig. 3b. Except for NiPS, they all contain precious

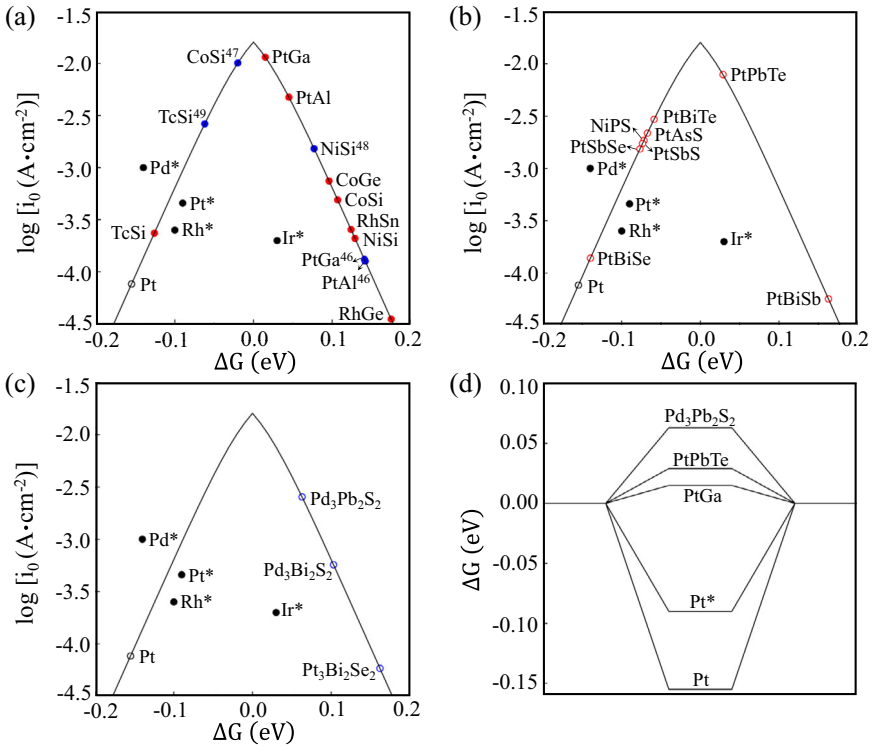

Fig. 3 | Volcano plots. a Volcano plot of binary HDTMs with space group $P2_13$. The red solid dots represent the results of this work, and the blue ones are the results of other previous work[46–49]. **b** Volcano plot of ternary HDTMs with space group $P2_13$. The red hollow dots show the results in this work. **c** Volcano plot of HDTMs with space group $I2_13$. The blue hollow dots show the results in this work. In all the figures above, the black solid and hollow dots represent experimental results and calculated Pt in this work, respectively. **d** Reaction coordinate diagram of three representatives, PtGa, PtPbTe, and $Pd_3Pb_2S_2$, which are the best candidates of catalyst for each kind of HDTMs.

metals Pt that play a unique role in catalysis. Finally, in the candidates with space group $I2_13$ predicted theoretically as high-fold degenerate TSMs, both $Pd_3Pb_2S_2$ and $Pd_3Bi_2S_2$ can exhibit excellent performance in HER according to the volcano plot in Fig. 3c. It is evident that the representatives PtGa, PtPbTe, and $Pd_3Pb_2S_2$ located at the peak of the volcano plots of three TSM types are the best choices for catalysis. By comparing these three compounds and Pt in experiment and theory, illustrated in the reaction coordinate diagram (Fig. 3d), the Gibbs free energy of PtGa and PtPbTe have little difference and is the smallest among all the TSM candidates. Overall, we determine that 16 high-fold degenerate TSMs, of which 11 compounds contain precious metals, achieve high catalytic efficiency comparable to the traditional high-efficiency catalyst Pt by using high-throughput calculation.

For all the TSM candidates with Pt element except PtMg, the optimal adsorption sites are same, i.e., the top site of Pt. Meanwhile, they all represent good HER performance with $|\Delta G| \leq 0.163$ eV near the peak of the volcano plot. Thus, the Pt element in TSM candidates plays an indispensable role in the surface adsorption of hydrogen. Compared to Pt, the topological surface states of topological catalysts containing Pt can provide high-mobility electrons, enhancing the catalytic efficiency. The topological surface state dispersion and Fermi arc of (001) surface are analyzed systematically for the representatives PtGa and PtPbTe in Figs. 4a–d. The four-fold degenerate point at M and the six-fold degenerate point at R are projected into the high symmetry k-points $\overline{M}$ and $\overline{\Gamma}$ of the surface Brillouin zone, respectively. Although most of the topological surface states are merged into the bulk state, especially in PtPbTe, four surface states connecting the four-fold degenerate point $H^{\Gamma}_{PG/PPT}$ with Chern number −4 can be observed. For PtGa, the surface states mainly provided by Pt elements on surface, as shown in Supplementary Fig. S14, extend from the degenerate point about 0.1 eV below Fermi level to higher energy above Fermi level. The large energy window of topological states and extremely long Fermi arcs enable surface adsorption to adapt to greater changes in energy and momentum. Besides Pt, precious metal Pd also appears in some topological catalysts. For example, in $Pd_3B_2S_2$ (B=Bi or Pb), belonging to the third type of TSM with space group $I2_13$, the Pd atoms located in the top two atomic layers contribute to the H adsorption according to the differential charge density in Supplementary Fig. S13. Consistent with topological catalysts containing Pt element, when a compound containing Pd element hosts topological surface state correlated with Pd as shown in Figs. 4e, f, the catalytic performance is slightly improved compared with the traditional high-efficiency catalyst Pd.

In order to delve into the effect of topological surface state in the high-efficiency topological catalysts, the surfaces with and without topological surface states for CoSi unrelated to the precious metals, are established when H is adsorbed on the catalyst. It has been verified in experiment that the Fermi arcs can emerge in (001) surface, but not in (111) surface in high-degenerate TSM CoSi[54]. In the [111] direction, similar to topological catalyst PtGa in Supplementary Fig. S5, there are three possible surfaces with Co-layer, Si-layer, or CoSi-layer. The optimal adsorption sites in (111) surfaces conform the symmetry of crystal well, such as Co-layer with the hole site of three Co atoms in Figs. 5a, b. The absolute value of Gibbs free energy $|\Delta G|$ of (111) surface with Co-layer, Si-layer, and CoSi-layer is respectively calculated to be −0.874 eV, 0.208 eV, and −0.243 eV, and larger than $|\Delta G|$ of (001) surface as illustrated in Fig. 5c. Thereafter, the topological surface states in (001) and (111) surface of CoSi are also calculated in Figs. 5d, e. The topological Fermi arcs of (001) surface are observed to connect high-fold degenerate points clearly, whereas no topological surface state exists in (111) surface because two high-fold degenerate points with opposite Chern number projected into same point $\overline{\Gamma}$. The fact that catalytic performance of the surface with topological surface state is better than that of the surface without nontrivial state in CoSi indicates that the topological surface states in high-fold degenerate topological catalysts indeed optimize the catalytic performance in HER.

Considering the stability of topological materials and the high-mobility electrons provided by topological surface states, topological catalysts have an advantage over other kinds of catalysts in electrochemical reactions. Referring to the outstanding HER catalytic performance of high-fold degenerate TSMs with chiral structures, which have extremely long topological surface states in k-space, we have discovered 16 high-fold degenerate topological HER catalysts whose catalytic activity is not inferior to that of traditional high-efficiency catalyst Pt. Among them, only 5 compounds have been predicted theoretically, and PtGa, PtAl, and CoSi have been verified experimentally. Based on the study of 11 topological catalysts containing precious metals Pt, Pd, or Rh, the topological surface states mainly formed by the d orbits of the precious metals can enhance catalytic efficiency. Almost all the high-fold degenerate TSMs containing Pt element in our database exhibit excellent HER catalytic performance, indicating that high-

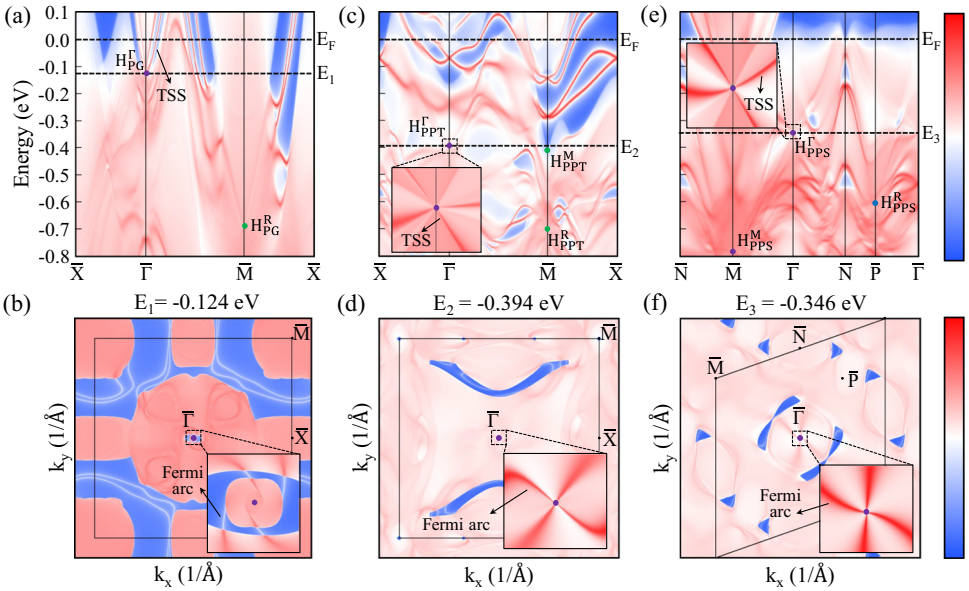

Fig. 4 | The (001) topological surface states (TSS). **a** Surface dispersion of binary HDTM PtGa. **b** Topological Fermi arcs of binary HDTM PtGa with energy fixed at the energy E_1 of four-fold degenerate fermion H^{Γ}_{PG}. **c** Surface dispersion of ternary HDTM PtPbTe. **d** Topological Fermi arcs of ternary HDTM PtPbTe with energy fixed at the energy E_2 of four-fold degenerate fermion H^{Γ}_{PPT}. **e** Surface dispersion of HDTMs $Pd_3Pb_2S_2$. **f** Topological Fermi arcs of HDTMs $Pd_3Pb_2S_2$ with energy fixed at the energy E_3 of four-fold degenerate fermion H^{Γ}_{PPS}. The green, blue, and red dots are four-fold, six-fold, and three-fold degenerate fermion, respectively.

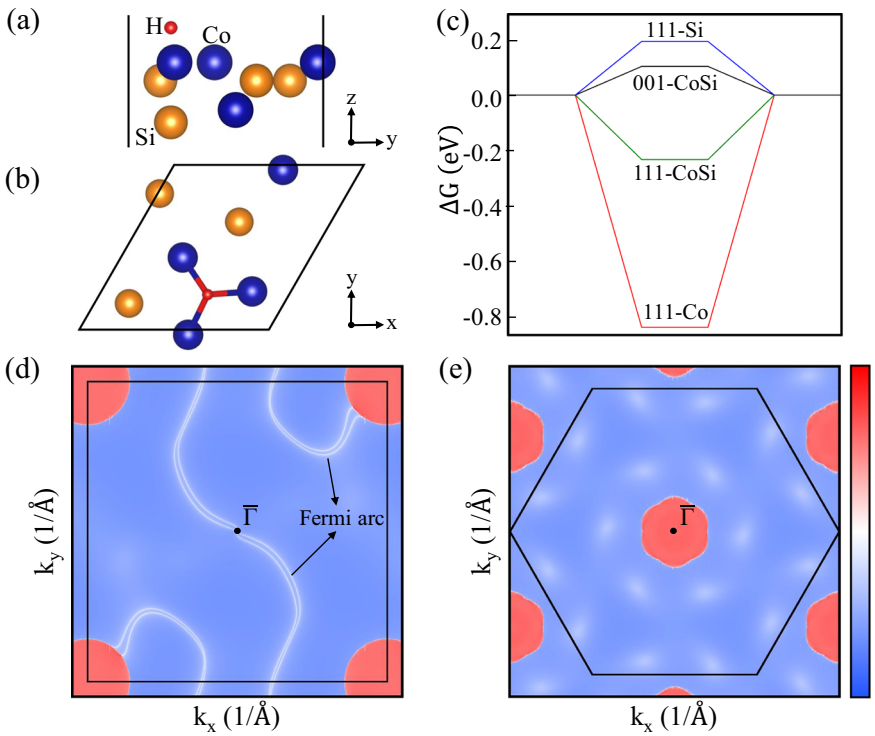

Fig. 5 | The (111) surface of CoSi. a, **b** The side and top views of stable adsorption site on (111) surface with Co-layer. **c** Reaction coordinate diagram when H is adsorbed on (001) surface and (111) surface with Co-layer, Si-layer, and CoSi-layer. **d**, **e** The constant energy surfaces of (001) and (111) surfaces, respectively, in case the energy is fixed at the energy of the high-fold degenerate point.

efficiency HER catalyst design can be achieved by synthesizing TSMs using monometallic catalysts. Meanwhile, 5 topological catalysts without precious metals, namely CoSi, CoGe, TcSi, NiSi, and NiPS, can also exhibit excellent HER catalytic performance, making it possible to greatly reduce the cost of catalysts. Most importantly, by comparing (001) surface and (111) surface with and without topological surface states in CoSi, the adsorption of H atoms on the surface with topological surface states exhibits smaller absolute value of Gibbs free energy. The significance of topological surface states providing high-mobility electrons is intuitively verified to improve catalytic efficiency. Therefore, this work not only significantly expands the number of topological HER catalysts and promotes their industrial application, but also theoretically validates the importance of topological surface states in topological catalysis, which also potentially leads to efficient topological catalysts in crucial electrocatalytic reactions beyond HER, such as the oxygen evolution reaction (OER) or CO_2 reduction.

Methods

The density functional theory (DFT) calculations have been conducted in the Vienna Ab Initio Simulation Package (VASP)[55] with the Perdew–Burke–Ernzerhof (PBE)[56] exchange-correlation functional. The cut-

off energy for plane-wave basis is 400 eV. The Monkhorst-Pack k-mesh for bulk and supercell calculations in self-consistent process are $8 \times 8 \times 8$ and $8 \times 8 \times 2$, respectively. All the lattice constants are fully relaxed. The spin-orbit coupling (SOC) is considered from self-consistent field calculations throughout the work. In order to investigate the topological surface states of high-fold degenerate TSMs, the maximally localized Wannier functions (MLWF)[57] are used to generate the tight-binding Hamiltonian based on the orbits near Fermi level. Afterwards, the Green's function method[58,59] is used to calculate the surface states by establishing a half-infinite boundary model. The topological invariants are calculated by using the WannierTools package[60].

For the surface modeling, a slab with $(1 \times 1 \times 3)$ unit cell for ternary compounds with space group $P2_13$ and $(1 \times 1 \times 4)$ unit cell for binary compounds with space group $P2_13$ and $I2_13$ is constructed. A 12 Å vacuum slab in the direction perpendicular to the surface for adsorbing is applied to avoid the periodic interaction. The atomic positions of the top layer of supercells are fully relaxed until the force on each atom is less than 10^{-3} eV/Å. Thus, according to the adsorption process $M+H^{+}+e^{-} \rightarrow M\text{-}H$, the adsorption energy could be calculated by

$$\Delta E = E_{M-H} - E_{sc} - \frac{1}{2}E_{H_2} \quad (1)$$

where $E_M - H$, E_{sc}, and E_{H_2} represent the total energy of adsorption system M-H including TSM supercell and adsorbate *H, TSM supercell M without adsorbate, and isolated adsorbate molecule H_2, respectively. Here, the energy of adsorbate atom *H is approximated as half of E_{H_2}. Furthermore, the Gibbs free energies are calculated by

$$\Delta G = \Delta E + \Delta ZPE - T\Delta S = \Delta E + 0.24\,eV \quad (2)$$

where ΔE is the adsorption energy, ΔZPE is the difference of zero-point energy between adsorbed and gas phase, ΔS is the entropy of adsorption of H, which is taken as half of the entropy of hydrogen at standard conditions, and T is the room temperature. The value of ΔZPE is calculated to be 0.04 eV for H/Cu(111)[11], and then applied to all compounds in this work since the vibrational frequencies have been found to depend much less on the metal than the bond strength[61].

Data availability

The datasets generated during and/or analysed during the current study are available from the corresponding author on reasonable request.

Received: 12 January 2026; Accepted: 12 March 2026;
Published online: 26 March 2026

References

1. Turner, J. A. Sustainable hydrogen production. *Science* **305**, 72–974 (2004).
2. Strmcnik, D., Lopes, P. P., Genorio, B., Stamenkovic, V. R. & Markovic, N. M. Design principles for hydrogen evolution reaction catalyst materials. *Nano Energy* **29**, 29–36 (2016).
3. Zhang, W. et al. Water electrolysis toward elevated temperature: advances, challenges and frontiers. *Chem. Rev.* **123**, 7119–7192 (2023).
4. Falcone, P. M., Hiete, M. & Sapio, A. Hydrogen economy and sustainable development goals: review and policy insights. *Curr. Opin. Green. Sustain. Chem.* **31**, 100506 (2021).
5. Capurso, T., Stefanizzi, M., Torresi, M. & Camporeale, S. M. Perspective of the role of hydrogen in the 21st century energy transition. *Energy Convers. Manag.* **251**, 114898 (2022).
6. Zhang, H. T., Sun, Z. X. & Hu, Y. H. Steam reforming of methane: current states of catalyst design and process upgrading. *Renew. Sustain. Energy Rev.* **149**, 111330 (2021).
7. LeRoy, R. L. Industrial water electrolysis: present and future. *Int. J. Hydrog. Energy* **8**, 401–417 (1983).
8. Wang, S., Lu, A. L. & Zhong, C. J. Hydrogen production from water electrolysis: role of catalysts. *Nano Converg.* **8**, 4 (2021).
9. Greeley, J., Jaramillo, T. F., Bonde, J., Chorkendorff, I. & Nørskov, J. K. Computational high-throughput screening of electrocatalytic materials for hydrogen evolution. *Nat. Mater.* **5**, 909–913 (2006).
10. Seh, Z. W. et al. Combining theory and experiment in electrocatalysis: Insights into materials design. *Science* **355**, eaad4998 (2017).
11. Nørskov, J. K. et al. Trends in the exchange current for hydrogen evolution. *J. Electrochem. Soc.* **152**, J23 (2005).
12. Yang, X. F. et al. Single-atom catalysts: a new frontier in heterogeneous catalysis. *Acc. Chem. Res.* **46**, 1740–1748 (2013).
13. Pu, Z. H. et al. Single-atom catalysts for electrochemical hydrogen evolution reaction: Recent advances and future perspectives. *Nano Micro Lett.* **12**, 21 (2020).
14. Zhao, G. Q., Rui, K., Dou, S. X. & Sun, W. P. Heterostructures for electrochemical hydrogen evolution reaction: a review. *Adv. Funct. Mater.* **28**, 1803291 (2018).
15. Gao, G. L., Zhu, G., Chen, X. L., Sun, Z. X. & Cabot, A. Optimizing Pt-based alloy electrocatalysts for improved hydrogen evolution performance in alkaline electrolytes: a comprehensive review. *ACS Nano* **17**, 20804–20824 (2023).
16. Hasan, M. Z. & Kane, C. L. Colloquium: topological insulators. *Rev. Mod. Phys.* **82**, 3045 (2010).
17. Qi, X. L. & Zhang, S. C. Topological insulators and superconductors. *Rev. Mod. Phys.* **83**, 1057 (2011).
18. Zhang, H. J. et al. Topological insulators in Bi_2Se_3, Bi_2Te_3 and Sb_2Te_3 with a single Dirac cone on the surface. *Nat. Phys.* **5**, 438 (2009).
19. Yan, B. H. & Felser, C. Topological materials: Weyl semimetals. *Annu. Rev. Condens. Matter Phys.* **8**, 337 (2017).
20. Armitage, N. P., Mele, E. J. & Vishwanath, A. Weyl and Dirac semimetals in three dimensional solids. *Rev. Mod. Phys.* **90**, 015001 (2018).
21. Li, G. W. & Felser, C. Heterogeneous catalysis at the surface of topological materials. *Appl. Phys. Lett.* **116**, 070501 (2020).
22. Xie, R. K., Zhang, T., Weng, H. M. & Chai, G. L. Progress, advantages, and challenges of topological material catalysts. *Small Sci.* **2**, 2100106 (2022).
23. Luo, H. X., Yu, P. F., Li, G. W. & Yan, K. Topological quantum materials for energy conversion and storage. *Nat. Rev. Phys.* **4**, 611–624 (2022).
24. Yang, Q., Zhang, Y. D., Sun, Y., Felser, C. & Li, G. W. Topological catalysis in the language of chemistry. *Innov. Mater.* **1**, 100013 (2023).
25. Wang, L. R. et al. Excellent catalytic performance toward the hydrogen evolution reaction in topological semimetals. *EcoMat* **5**, e12316 (2023).
26. Wan, X. G., Turner, A. M., Vishwanath, A. & Savrasov, S. Y. Topological semimetal and Fermi-arc surface states in the electronic structure of pyrochlore iridates. *Phys. Rev. X* **83**, 205101 (2011).
27. Weng, H. M., Fang, C., Fang, Z., Bernevig, B. A. & Dai, X. Weyl semimetal phase in noncentrosymmetric transition-metal monophosphides. *Phys. Rev. X* **5**, 011029 (2015).
28. Xu, S. Y. et al. Discovery of a Weyl fermion semimetal and topological Fermi arcs. *Science* **349**, 613–617 (2015).
29. Lv, B. Q. et al. Experimental discovery of Weyl semimetal TaAs. *Phys. Rev. X* **5**, 031013 (2015).
30. Liu, E. K. et al. Giant anomalous Hall effect in a ferromagnetic kagome-lattice semimetal. *Nat. Phys.* **14**, 1125 (2018).
31. Wang, Q. et al. Large intrinsic anomalous Hall effect in half-metallic ferromagnet $Co_3Sn_2S_2$ with magnetic Weyl fermions. *Nat. Commun.* **9**, 3681 (2018).
32. Liu, D. F. et al. Magnetic Weyl semimetal phase in a Kagomé crystal. *Science* **365**, 1282 (2019).
33. Morali, N. et al. Fermi-arc diversity on surface terminations of the magnetic Weyl semimetal $Co_3Sn_2S_2$. *Science* **365**, 1286 (2019).
34. Young, S. M. et al. Dirac semimetal in three dimensions. *Phys. Rev. Lett.* **108**, 140405 (2012).
35. Wang, Z. J. et al. Dirac semimetal and topological phase transitions in A_3Bi (A = Na, K, Rb). *Phys. Rev. B* **85**, 195320 (2012).

36. Burkov, A. A., Hook, M. D. & Balents, L. Topological nodal semimetals. *Phys. Rev. B* **84**, 235126 (2011).
37. Bradlyn, B. et al. Beyond Dirac and Weyl fermions: unconventional quasiparticles in conventional crystals. *Science* **353**, aaf5037 (2016).
38. Tang, P. Z., Zhou, Q. & Zhang, S. C. Multiple types of topological fermions in transition metal silicides. *Phys. Rev. Lett.* **119**, 206402 (2017).
39. Li, L. Q., Zeng, J., Qin, W., Cui, P. & Zhang, Z. Y. Tuning the hydrogen activation reactivity on topological insulator heterostructures. *Nano Energy* **58**, 40–46 (2019).
40. Rajamathi, C. R. et al. Weyl semimetals as hydrogen evolution catalysts. *Adv. Mater.* **29**, 1606202 (2017).
41. Li, J. X. et al. Topological quantum catalyst: Dirac nodal line states and a potential electrocatalyst of hydrogen evolution in the TiSi family. *Sci. China Mater.* **61**, 23–29 (2018).
42. Li, G. W. et al. Dirac nodal arc semimetal $PtSn_4$: an ideal platform for understanding surface properties and catalysis for hydrogen evolution. *Angew. Chem.* **131**, 13241–13246 (2019).
43. Li, G. W. et al. Surface states in bulk single crystal of topological semimetal $Co_3Sn_2S_2$ toward water oxidation. *Sci. Adv.* **5**, eaaw9867 (2019).
44. Li, J. et al. Enhanced electrocatalytic hydrogen evolution from large-scale, facile-prepared, highly crystalline WTe_2 nanoribbons with Weyl semimetallic phase. *ACS Appl. Mater. Interfaces* **10**, 458–467 (2018).
45. He, Y. et al. Topologically nontrivial 1T'-$MoTe_2$ as highly efficient hydrogen evolution electrocatalyst. *J. Phys. Mater.* **4**, 014001 (2021).
46. Yang, Q. et al. Topological engineering of Pt-group-metal-based chiral crystals toward high-efficiency hydrogen evolution catalysts. *Adv. Mater.* **32**, 1908518 (2020).
47. He, Y. et al. Discovery and facile synthesis of a new silicon based family as efficient hydrogen evolution reaction catalysts: a computational and experimental investigation of metal monosilicides. *Small* **17**, 2006153 (2021).
48. Liu, W. et al. Theoretical realization of hybrid Weyl state and associated high catalytic performance for hydrogen evolution in NiSi. *iScience* **25**, 103543 (2022).
49. Zhan, J. et al. Design of high-efficiency hydrogen evolution catalysts in a chiral crystal. *ACS Catal.* **14**, 1030–1036 (2024).
50. Wang, Y., Yang, W. W., Shi, W. J., Liu, W. J. & Xu, Q. N. Exhaustive screening of high-fold degenerate topological semimetal with chiral structure. *npj Couput. Mater.* **11**, 120 (2025).
51. Chen, H. et al. Promoting subordinate, efficient ruthenium sites with interstitial silicon for Pt-Like electrocatalytic activity. *Angew. Chem. Int. Ed.* **58**, 11409–11413 (2019).
52. Chen, H. et al. Screening and understanding lattice silicon-controlled catalytically active site motifs from a library of transition metal-silicon intermetallics. *Small* **18**, 2107371 (2022).
53. Lv, B. Q. et al. Observation of multiple types of topological fermions in PdBiSe. *Phys. Rev. B* **99**, 201104 (2019).
54. Yuan, Q. Q. et al. Quasiparticle interference evidence of the topological Fermi arc states in chiral fermionic semimetal CoSi. *Sci. Adv.* **5**, eaaw9485 (2019).
55. Kresse, G. G. & Furthmüller, J. Efficient iterative schemes for ab initio total-energy calculations using a plane-wave basis set. *Phys. Rev. B* **54**, 11169–11186 (1996).
56. Perdew, J. P., Burke, K. & Ernzerhof, M. Generalized gradient approximation made simple. *Phys. Rev. Lett.* **77**, 3865–3868 (1996).
57. Marzari, N. & Vanderbilt, D. Maximally localized generalized Wannier functions for composite energy bands. *Phys. Rev. B* **56**, 12847–12865 (1997).
58. Sancho, M. P. L., Sancho, J. M. L. & Rubio, J. Quick iterative scheme for the calculation of transfer matrices: application to Mo (100). *J. Phys. F Met. Phys.* **14**, 1205–1215 (1984).
59. Sancho, M. P. L., Sancho, J. M. L. & Rubio, J. Highly convergent schemes for the calculation of bulk and surface Green functions. *J. Phys. F Met. Phys.* **15**, 851–858 (1985).
60. Wu, Q. S., Zhang, S. N., Song, H. F., Troyer, M. & Soluyanov, A. A. WannierTools: an open-source software package for novel topological materials. *Comput. Phys. Commun.* **224**, 405–416 (2018).
61. Pedersen, T. B. et al. On the compensation effect in heterogeneous catalysis. *J. Phys. Chem. B* **107**, 9325 (2003).

Acknowledgements

Q.N. Xu thanks G.Xu. and J.Z. Zhao for fruitful discuss. This work is supported by the National Key R&D Program of China (Grants No. 2023YFA1506901), the National Natural Science Foundation of China (NSFC) (Grants No. 12374160), the Natural Science Foundation of Shandong Province (Grants No. 2023HWYQ-009), and the Taishan Scholar Program of Shandong Province (Grants No. tsqn202306039).

Author contributions

Y.W. collected the data, wrote the codes, and did the calculations. Q.X. initialized this project and designed the workflow. H.Y. and W.L. gave scientific advice. Y.W. and Q.X. wrote the manuscript with contributions from all authors.

Competing interests

The authors declare no competing interests.

Additional information

Supplementary information The online version contains supplementary material available at https://doi.org/10.1038/s42004-026-01985-w.

Correspondence and requests for materials should be addressed to Qiunan Xu.

Peer review information *Communications Chemistry* thanks Hui Chen and the other, anonymous, reviewer(s) for their contribution to the peer review of this work.